HAL open science

Minimizing the Discrimination Time for Quantum States of an Artificial Atom

I Takmakov, P Winkel, F Foroughi, L Planat, D Gusenkova, M Spiecker, D Rieger, L Grünhaupt, A V Ustinov, W Wernsdorfer, et al.

To cite this version:

I Takmakov, P Winkel, F Foroughi, L Planat, D Gusenkova, et al.. Minimizing the Discrimination Time for Quantum States of an Artificial Atom. Physical Review Applied, 2021, 15 (6), pp.064029. 10.1103/physrevapplied.15.064029 . hal-04158340

HAL Id: hal-04158340

https://hal.science/hal-04158340v1

Submitted on 11 Jul 2023

HAL is a multi-disciplinary open access archive for the deposit and dissemination of scientific research documents, whether they are published or not. The documents may come from teaching and research institutions in France or abroad, or from public or private research centers.

L'archive ouverte pluridisciplinaire **HAL**, est destinée au dépôt et à la diffusion de documents scientifiques de niveau recherche, publiés ou non, émanant des établissements d'enseignement et de recherche français ou étrangers, des laboratoires publics ou privés.

Minimizing the Discrimination Time for Quantum States of an Artificial Atom

I. Takmakov,[1,2,3,4,*,†] P. Winkel,[1,2,†] F. Foroughi,[5,6] L. Planat,[5,6] D. Gusenkova,[1] M. Spiecker,[1] D. Rieger,[1] L. Grünhaupt,[1] A.V. Ustinov,[1,4] W. Wernsdorfer,[1,2,3] I.M. Pop,[1,2,3] and N. Roch[5,6]

[1] *Physikalisches Institut, Karlsruhe Institute of Technology, Karlsruhe 76131, Germany*
[2] *IQMT, Karlsruhe Institute of Technology, Eggenstein-Leopoldshafen 76344, Germany*
[3] *Institute of Nanotechnology, Karlsruhe Institute of Technology, Eggenstein Leopoldshafen 76344, Germany*
[4] *Russian Quantum Center, National University of Science and Technology MISIS, Moscow 119049, Russia*
[5] *CNRS, Institut NEEL, Grenoble F-3800, France*
[6] *Université Grenoble Alpes, Institut NEEL, Grenoble F-3800, France*

(Received 23 November 2020; revised 2 March 2021; accepted 5 May 2021; published 11 June 2021)

Fast discrimination between quantum states of superconducting artificial atoms is an important ingredient for quantum information processing. In circuit quantum electrodynamics, increasing the signal-field amplitude in the readout resonator, dispersively coupled to the artificial atom, improves the signal-to-noise ratio and increases the measurement strength. Here, we employ this effect over 2 orders of magnitude in readout power, made possible by the unique combination of a dimer-Josephson-junction-array amplifier with a large dynamic range and the fact that the readout of our granular aluminum fluxonium artificial atom remains quantum nondemolition (QND) at relatively large photon numbers in the readout resonator, up to $\bar{n} = 110$. Using Bayesian inference, this allows us to detect quantum jumps faster than the readout-resonator response time $2/\kappa$, where κ is the bandwidth of the readout resonator.

DOI: 10.1103/PhysRevApplied.15.064029

I. INTRODUCTION

Quantum jumps—transitions between discrete energy levels of a quantum system—have been measured over the past two decades in various physical systems [1–6]. The measurement of quantum jumps relies on the ability to discriminate the individual states of a quantum system on a time scale significantly shorter than their energy-relaxation times. For applications in quantum technologies, this ability is instrumental in the implementation of quantum error correction algorithms [7–11], a milestone on the quantum information processing road map, or can be used as a detection tool informing on the interactions between the quantum system and its environment [12–14]. For all these applications, it is important to discriminate between the states of a quantum system as quickly as possible.

The speed of quantum-nondemolition (QND) readout in circuit quantum electrodynamics [15–18] improved significantly over the past decade [19–22], mainly due to the development of near-quantum-limited Josephson parametric amplifiers [23–29], which increase the signal-to-noise ratio (SNR) by reducing the noise of the measurement setup down to the quantum limit [30]. An additional resource to speed up the measurement, the increase of the readout drive power, has barely been exploited as yet, because superconducting qubits are observed to suffer from increased energy relaxation and leakage out of computational space when the circulating photon number in the resonator, $\bar{n}$, is increased. In practice, these effects bound the photon number for QND readout [21,31–33], typically to $\bar{n} < 10$, for reasons that are currently the subject of theoretical investigation [34–36].

By performing a continuous measurement and benefiting from the remarkable insensitivity to $\bar{n}$ of a granular aluminum (grAl) fluxonium [37] artificial atom, recently reported in Ref. [38], we demonstrate a significant decrease of the QND state discrimination time with increasing $\bar{n}$, up to $\bar{n} = 110$. To handle the correspondingly large signal power, we use a high-dynamic-range dimer-Josephson-junction-array parametric amplifier (DJJAA) [39]. We are able to reduce the mean time required to discriminate between the qubit states from 1.2 μs at $\bar{n} = 1.7$ photons, down to 0.175 μs at $\bar{n} = 56$ photons, which is shorter than the time required for the resonator pointer state to transition between the steady states corresponding to the qubit population. This discrimination time is not limited by the integration time for the quadrature decomposition of the readout signal—which, in principle can be made arbitrarily short—but by the onset of squeezing caused by the nonlinearity of the readout resonator and the increasing excitation of higher-energy eigenstates of

*ivan.takmakov@kit.edu
†These authors contributed equally to this work.

 © 2021 American Physical Society

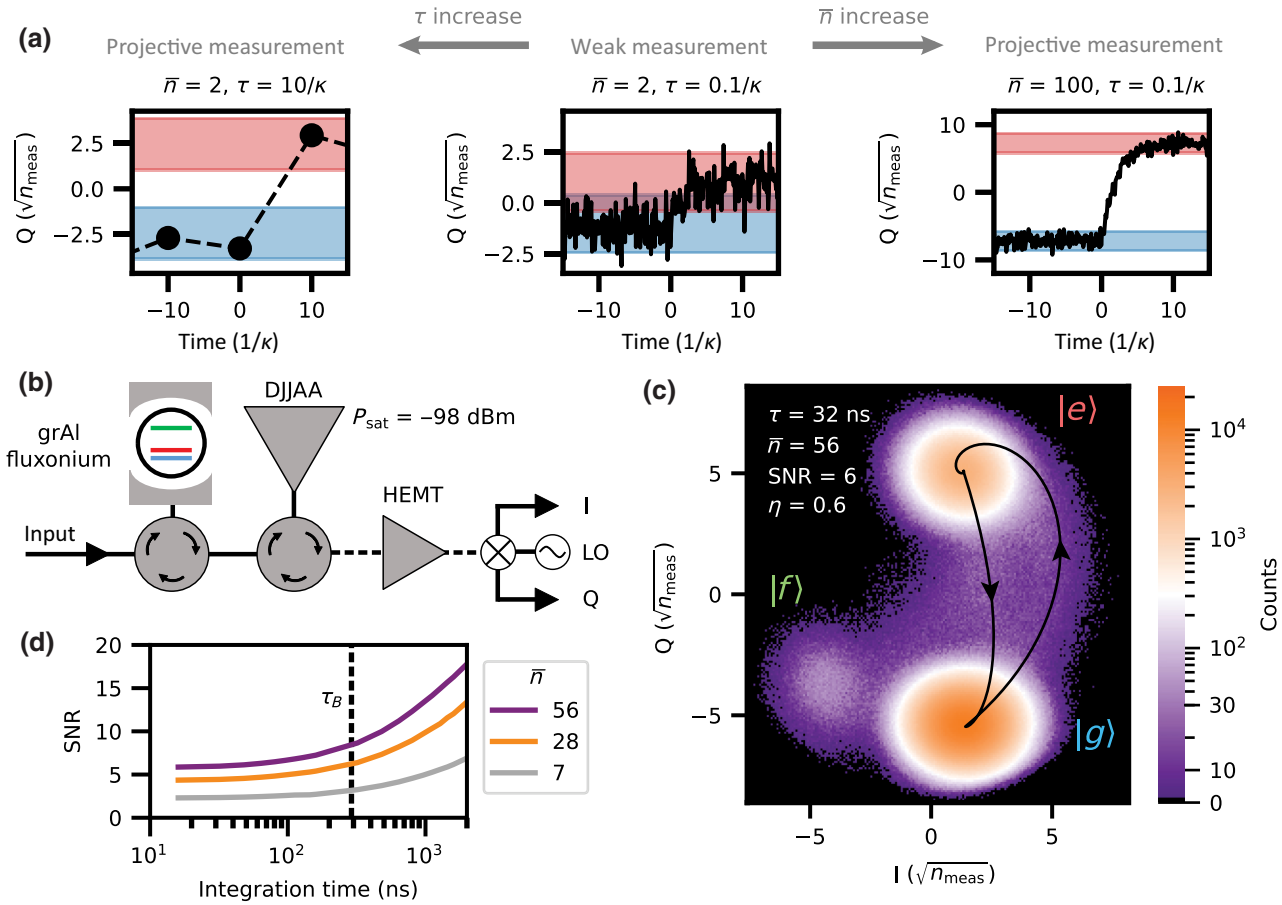

FIG. 1. (a) The simulated Q quadrature (black lines) of a quantum-limited continuous measurement of a qubit coupled to a readout resonator. The quadrature values are presented in units of the square root of the measurement photons $\sqrt{n_{\text{meas}}} = \sqrt{\bar{n}B^{-1}\kappa/4}$, where $\bar{n}$ is the circulating photon number in the readout resonator, κ is the coupling rate of the resonator to the measurement apparatus, and $B^{-1} \approx \tau + \tau_B$ is the measurement bandwidth, given by the sum of the integration time τ and the resonator response time $\tau_B = 2/\kappa$ (see Appendix A). The blue and red areas indicate $\pm 2\sigma$ intervals centered around the mean values of the Q quadrature corresponding to the ground and first excited state, respectively, denoted $Q_{|g\rangle}$ and $Q_{|e\rangle}$. The panels depict the transition from a weak measurement (center) to a projective measurement by increasing either τ (left panel) or $\bar{n}$ (right panel). (b) A simplified schematic of the experimental setup. The incident readout signal reflects from a resonator coupled to a fluxonium artificial atom, both implemented using grAl, which is the same device as discussed in Ref. [38]. The reflected signal is amplified by a dimer-Josephson-junction-array amplifier (DJJAA) [39] operated in the nondegenerate phase-preserving regime. The measured 1-dB compression point of the DJJAA at 20 dB of power gain is $P_{\text{sat}} = -98$ dBm (see Appendix A). The signal is further amplified by a commercial high-electron-mobility transistor amplifier (HEMT) thermalized at 4 K and is demodulated at room temperature into the I and Q quadratures. (c) A two-dimensional (2D) histogram of the continuously measured in-phase (I) and out-of-phase (Q) quadratures, presented in units of the square root of the measurement photons $\sqrt{n_{\text{meas}}} = \sqrt{\bar{n}B^{-1}\kappa/4}$, where $\bar{n} = 56$ and $B^{-1} = 322$ ns. In order to highlight the resonator classical trajectories, the colorbar scale is linear below 30 counts and logarithmic above. The calculated trajectories ($|g\rangle$ to $|e\rangle$ and back) corresponding to the linear response of the resonator are indicated by the black traces. The SNR, defined by Eq. (1), is 6 and the obtained quantum efficiency for individual pointer-state measurements is $\eta = 0.6 \pm 0.1$ (see Appendix A). (d) The SNR measured as a function of the integration time τ for different $\bar{n}$ values. The black dotted line corresponds to τ_B.

the artificial atom. Since the integration time is significantly shorter than the $\tau_B = 290$ ns response time of the readout resonator, we employ Bayesian filtering [9,40–45] to detect quantum jumps before the system reaches a new steady state.

II. RESULTS

During the continuous measurement of a qubit coupled to a readout resonator, schematically shown in Fig. 1(a), when the qubit state changes between ground ($|g\rangle$) and excited ($|e\rangle$), due to thermal or nonequilibrium (e.g., quasiparticles [13]) excitations, the readout-signal quadrature evolves as $Q(t) - Q_{|e\rangle} \propto \left(Q_{|g\rangle} - Q_{|e\rangle}\right) e^{-\kappa t/2}$. Here, $Q_{|g\rangle/|e\rangle}$ are the measured readout-resonator quadrature values [see Fig. 1(b)] of the steady states corresponding to $|g\rangle$ and $|e\rangle$ (see Appendix A). The resonator bandwidth κ sets the response time $\tau_B = 2/\kappa$ of the measurement apparatus to a quantum jump. The readout power,

TABLE I. A list of the qubit-resonator-circuit parameters. The Josephson energy E_J is *in situ* flux tunable via the SQUID junction. The flux bias for the fluxonium qubit is fine tuned in the vicinity of $\Phi_0/2$ to maximize the pointer-state separation.

E_C/h (GHz)	2.8
E_L/h (GHz)	0.71
E_J/h (GHz)	7.1
Fluxonium flux bias, Φ_0	0.542
$\kappa/2\pi$ (MHz)	1.1
f_{res} (GHz)	7.247
$\chi_{\mathrm{ge}}/2\pi$ (MHz)	−1.09
f_{ge} (MHz)	902
f_{ef} (MHz)	7701
T_1 (μs)	20 ± 4

populating the readout resonator with $\bar{n}$ photons, and the integration time τ determine whether a single measured quadrature point is sufficient (projective measurement) or insufficient (weak measurement) to determine the qubit state. A typical example of a sequence of weak measurements is shown in the middle panel of Fig. 1(a). It can be converted to a strong measurement either by increasing τ [left panel of Fig. 1(a)], which unfortunately reduces the time resolution of the qubit state determination, or by increasing $\bar{n}$ [right panel of Fig. 1(a)]. While the quadrature response time of the readout resonator is limited to τ_B, given a sufficiently large SNR, the qubit state can be inferred before the quadrature reaches its steady state. Therefore, as we show in the following, increasing $\bar{n}$ is a viable strategy to speed up qubit state detection, provided that the qubit and the measurement chain can handle the increased readout power.

Our experimental setup is shown in Fig. 1(b). The monitored quantum system is a fluxonium artificial atom [46], dispersively coupled via a shared inductance to a readout resonator (for the list of system parameters, see Table I). The inductors required for both the fluxonium and readout antenna are implemented using grAl [37] and the fluxonium junction is implemented in the shape of a superconducting quantum interference device (SQUID) [38,47]. The sample chip is placed in a rectangular waveguide, following the concept in Ref. [48], and measured in reflection [see Fig. 1(b)]. We use a DJJAA [39] to perform nondegenerate phase-preserving amplification [29,49] with 20 dB of power gain and 7 MHz instantaneous bandwidth. The DJJAA saturation power is −98 dBm (see Appendix A), corresponding to a circulating photon number in the readout resonator of $\bar{n} \approx 10^4$.

In Fig. 1(c), we show a typical histogram of the demodulated readout-resonator response for $\bar{n} = 56$ and an integration time $\tau = 32$ ns. The distribution shows three maxima, corresponding to the first three lowest-energy levels of the fluxonium artificial atom, labeled $|g\rangle$, $|e\rangle$, and $|f\rangle$. Since the integration time $\tau = 32$ ns is much shorter than the characteristic response time of the measurement setup $\tau_B = 290$ ns, trajectories corresponding to transitions between the three steady states are visible, filling the space between the maxima in the IQ plane. The steady states are visibly squeezed because of the intrinsic [50] and inherited nonlinearity of the grAl resonator (see Appendix B). In Fig. 1(d), we plot the measured SNR, defined as the ratio between the separation of the pointer states in the IQ plane and their variance,

$$\mathrm{SNR} = \frac{\left|\alpha_{|e\rangle} - \alpha_{|g\rangle}\right|}{\sigma_{|e\rangle} + \sigma_{|g\rangle}} = \sqrt{\frac{1}{4}\kappa\eta\bar{n}(\tau + \tau_B)}\sin\frac{\varphi_{eg}}{2}, \quad (1)$$

versus the integration time τ, where $\alpha_{|g\rangle,|e\rangle}$ are the pointer states, $\sigma_{|g\rangle,|e\rangle}$ are the corresponding variances, φ_{eg} is the phase difference between the pointer states, and $\eta = 0.6 \pm 0.1$ is the quantum efficiency (see Appendix A). Following Eq. (1), the SNR saturates when τ goes below τ_B, as discussed in Refs. [6,51]. The resonator response time can therefore significantly slow down the detection of quantum jumps based on fixed IQ thresholds, commonly used for latching filters (see Appendix C). However, since the state of the artificial atom is encoded in the instantaneous evolution of the pointer state, given a sufficient SNR it can be extracted even before the resonator reaches its steady state. Due to the increased SNR made available by measurements at large $\bar{n}$, as shown in Fig. 1(d), we can implement a recursive Bayesian filter for quantum-jump detection, assuming a hidden Markov model, similarly to Refs. [9,40–45]:

$$P_H(t+\tau) = \frac{P(\varphi_{t+\tau}, \varphi_t|H) \times P_H(t)}{\sum_{H'\in\{\mathrm{g,e,f}\}} P(\varphi_{t+\tau}, \varphi_t|H') \times P_{H'}(t)}, \quad (2)$$

$$P(\varphi_{t+\tau}, \varphi_t|H) = \exp\left[-\frac{\left[\varphi_{t+\tau} - \varphi_{t+\tau}^{\mathrm{calc}}(\varphi_t, H)\right]^2}{2\beta_H^2\sigma_H^2}\right]. \quad (3)$$

Here, $P_H(t+\tau)$ is the conditional probability for each fluxonium state hypothesis $H \in \{\mathrm{g,e,f}\}$, given that the pointer-state phases $\varphi_{t+\tau}$ and φ_t are measured at times $t+\tau$ and t, respectively. Equation (2) updates the probabilities for each fluxonium state H in time increments of the integration time τ. Following Eq. (3), the unnormalized probability $P(\varphi_{t+\tau}, \varphi_t|H)$ is a Gaussian with standard deviation $\beta_H\sigma_H$ and mean value $\varphi_{t+\tau}^{\mathrm{calc}}(\varphi_t, H)$, where σ_H is the variance of the pointer states, $\beta_H \in (0.8, 1.2)$ is a coefficient tuning the filter responsivity, and $\varphi_{t+\tau}^{\mathrm{calc}}(\varphi_t, H)$ is the phase corresponding to the classical trajectory starting at a pointer state with φ_t and ending at the steady state corresponding to H (see Appendix C).

A typical detection sequence for quantum jumps between the $|e\rangle$, $|g\rangle$, and $|f\rangle$ fluxonium states using the recursive Bayesian filter of Eq. (2) is shown in Fig. 2(a).

Based on the measured black trace, the filter estimate for the fluxonium state is indicated by the white trace. Note that the $|e\rangle \rightarrow |f\rangle$ and $|f\rangle \rightarrow |e\rangle$ quantum jumps are correctly identified, even though the pointer state intersects the phase value corresponding to the $|g\rangle$ steady state. A quantum jump is declared once one of the probabilities surpasses 50%. The minimum probability for each state is typically capped at 10% to prevent the filter saturation at $P_H(t) = 0$, in which case Eq. (2) is no longer responsive. In Fig. 2(b), we select an example that illustrates the ability of the Bayesian filter to declare a $|g\rangle \rightarrow |e\rangle \rightarrow |g\rangle$ quantum-jump sequence for which the readout resonator never reaches the steady state associated with $|e\rangle$.

In Fig. 3, we compare the Bayesian state estimate to a simpler more commonly used latching filter (see Appendix C) for $|g\rangle \leftrightarrow |e\rangle$ transition. In Fig. 3(a), histograms of the jump detection times are shown for $\tau = 32$ ns. The Bayesian inference provides a 3.5 times faster state discrimination on average. In Fig. 3(b), the mean jump detection time is shown versus τ for both filters. As expected, the Bayesian detection starts to outperform the latching filter for $\tau < \tau_B$ (also see Fig. 6). The obtained measurement QND fidelity [52] $(P_{e|e} + P_{g|g})/2 = 98\%$ is comparable to the state-of-the-art [19,21,22,52,53], where $P_{e|e}$ and $P_{g|g}$ are the probabilities of obtaining the same result in consecutive measurements separated by Δt, is comparable to state-of-the-art [19,21,22,52,53]. The time interval $\Delta t = 432$ ns is chosen such that the detection time of 98% of all quantum jumps is less than Δt for the Bayesian filter. Transitions from $|e\rangle$ to $|g\rangle$ and $|f\rangle$ during Δt contribute 1% and 1.2%, respectively, to the value of $P_{e|e} = 96.7\%$ and transitions from $|g\rangle$ to $|e\rangle$ contribute 0.3% to the measured $P_{g|g} = 99.6\%$.

In Fig. 3(c), the average jump detection time for the $|e\rangle \rightarrow |g\rangle$ transition is shown as a function of $\bar{n}$. The results are obtained using the recursive Bayesian filter, since the latching filter detection time saturates at 620 ns [see Fig. 3(b)]. The detection time decreases with $\bar{n}$, as expected from Eq. (1), and it has a minimum of 175 ns for $\bar{n} = 56$. The increase at $\bar{n} = 110$ is caused mainly by the nonlinearity of the grAl readout resonator and the associated squeezing of the pointer-state distributions.

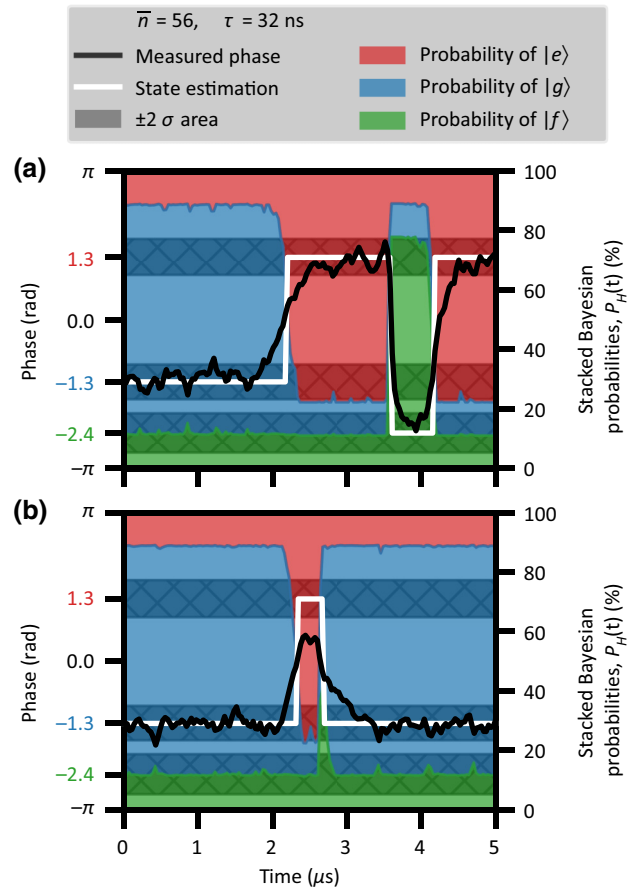

FIG. 2. Examples of Bayesian inference of the state of the artificial atom ($|g\rangle$, $|e\rangle$, or $|f\rangle$) based on the continuous-wave measurement of the readout resonator. The black lines represent the phase versus time extracted from the measured IQ response [see Fig. 1(b)] for $\bar{n} = 56$ and $\tau = 32$ ns. The hatched areas indicate the $\pm 2\sigma$ intervals for each state, centered on the corresponding average phase response: -1.3 for $|g\rangle$ (blue label), 1.3 for $|e\rangle$ (red label), and -2.4 for $|f\rangle$ (green label). The colored areas show the stacked bar plot versus time for the calculated Bayesian probabilities [see Eq. (2)] of the first three states of the artificial atom: $|g\rangle$ in blue, $|e\rangle$ in red, and $|f\rangle$ in green. The inferred quantum state is indicated by the white line; when one of the Bayesian probabilities reaches 50%, a jump to the respective state is declared.

III. SUMMARY

In summary, by exploiting the increasing SNR with $\bar{n}$, we demonstrate a decrease of the state detection time of the artificial atom. This is achieved by monitoring the transient trajectories in the IQ plane of the readout-resonator response, triggered by quantum jumps between the three lowest-energy states of the artificial atom. We show that quantum states can be discriminated by using a recursive Bayesian filter before the resonator reaches its steady state. In our case, the Bayesian filter is applied in postprocessing. However, one can imagine using more sophisticated filtering and potentially running it in real time by hardware encoding on an instrument based on field-programmable gate arrays (FPGAs) [54,55]. The main limiting factors for the $\bar{n}$ increase are the emergence of non-QND processes, the nonlinearity of the readout resonator, and the saturation of the parametric amplifier. Thus, the mitigation of non-QND processes during readout with increasing photon numbers could further increase the quantum state detection speed in both pulsed and continuous measurements.

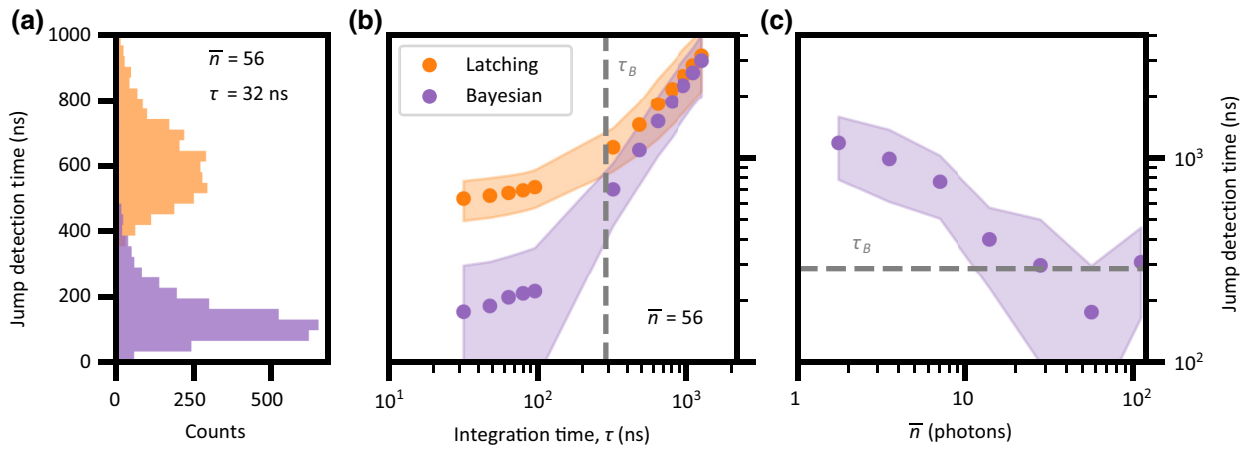

FIG. 3. (a) Histograms of the quantum-jump detection times obtained with a three-point latching filter (orange, see Appendix C and a recursive Bayesian filter (purple, see Eq. 2), for $|g\rangle \rightarrow |e\rangle$. For this histogram, $\bar{n} = 56$ and the integration time is $\tau = 32$ ns. (b) The average detection time for $|g\rangle \rightarrow |e\rangle$ jumps as a function of the integration time, obtained using the three-point latching filter (in orange) or the recursive Bayesian filter (in purple). The colored areas represent the standard deviation of the jump-detection-time distribution [see panel (a)]. (c) The quantum-jump detection time as a function of the photon number in the readout resonator $\bar{n}$, for $|g\rangle \rightarrow |e\rangle$ quantum jumps. The colored area represents the standard deviation of the jump-detection-time distribution [see panel (a)].

ACKNOWLEDGMENTS

Funding was provided by the Alexander von Humboldt foundation in the framework of a Sofja Kovalevskaja award endowed by the German Federal Ministry of Education and Research and by the Initiative and Networking Fund of the Helmholtz Association, within the Helmholtz Future Project "Scalable solid-state quantum computing." Furthermore, this research was supported by the Agence Nationale de la Recherche (ANR) under (Project No. ANR-16-CE24-0005). I.T. and A.V.U. acknowledge partial support from the Ministry of Education and Science of the Russian Federation in the framework of the Increase Competitiveness Program of the National University of Science and Technology MISIS (Contract No. K2-2020-017). The facilities use was supported by the KIT Nanostructure Service Laboratory (NSL). A.V.U., W.W., I.M.P., and N.R. acknowledge financial support from the Centre National de la Recherche Scientifique (CNRS) and the Karlsruhe Institute of Technology (KIT), through the international laboratory Superconducting Devices and Materials (SUPRADEVMAT) between the Grenoble and Karlsruhe campuses.

APPENDIX A: DIMER-JOSEPHSON-JUNCTION-ARRAY AMPLIFIER (DJJAA)

We utilize a DJJAA [39] that consists of an array of $N = 1600$ SQUIDs interrupted in the middle by an interdigitated capacitor [see Fig. 4(a)]. The capacitor breaks the symmetry between odd and even modes and creates pairs of modes [see Fig. 4(b)]. Each of these pairs, which we refer to as dimers, can be used for four-wave-mixing nondegenerate parametric amplification. In this regime, the signal and idler tones occupy different physical modes and the gain profile has a double-Lorentzian shape when the pump tone is applied in between the modes.

The parameters of the DJJAA (sample $N = 1600$ reported in Ref. [39]) are as follows: $I_J^{\mathrm{SQUID}} = 3.5\ \mu$A, $C_J = 1225$ fF, $C_0 = 0.45$ fF, $C_c = 40$ fF, and $C_0' = 33$ fF. The power gains presented in Fig. 4(d) are the lower-frequency lobes of the nondegenerate gain profiles (the pump-power-dependent lobe splitting is 260 ± 20 MHz). For 20 dB of gain, we obtain an instantaneous band of 7 MHz and a saturation power of -98 dBm [see Fig. 4(e)].

The measurement efficiency η is extracted by fitting the dependence of the steady-state SNR with the integration time

$$\mathrm{SNR_{SS}} = \frac{|\alpha|}{\sqrt{\sigma_Q^2 + \sigma_I^2}} = \sqrt{\kappa B^{-1} \eta \bar{n}/4}, \qquad \text{(A1)}$$

where α is the pointer state of the ground state and $\sigma_{I/Q}$ are its variances along respective quadratures [see Fig. 4(c)]. B^{-1} is the measurement bandwidth (see the Supplemental Material in Ref. [6]), which depends on all the measurement-setup bandwidths, including the integration time τ, the readout-resonator line width κ, the DJJAA bandwidth, etc. In our case, the main limiting factors are τ and κ; therefore, we can consider $B^{-1} \approx \tau + \tau_B$, where $\tau_B = 2/\kappa$. The $2/\kappa$ comes from the readout-resonator pointer-state evolution $\alpha(t) - \alpha_f \propto (\alpha_i - \alpha_f)\, e^{-\kappa t/2}$, where $\alpha_{\mathrm{f/i}}$ are the mean pointer states of the final and initial steady states (see Appendix C).

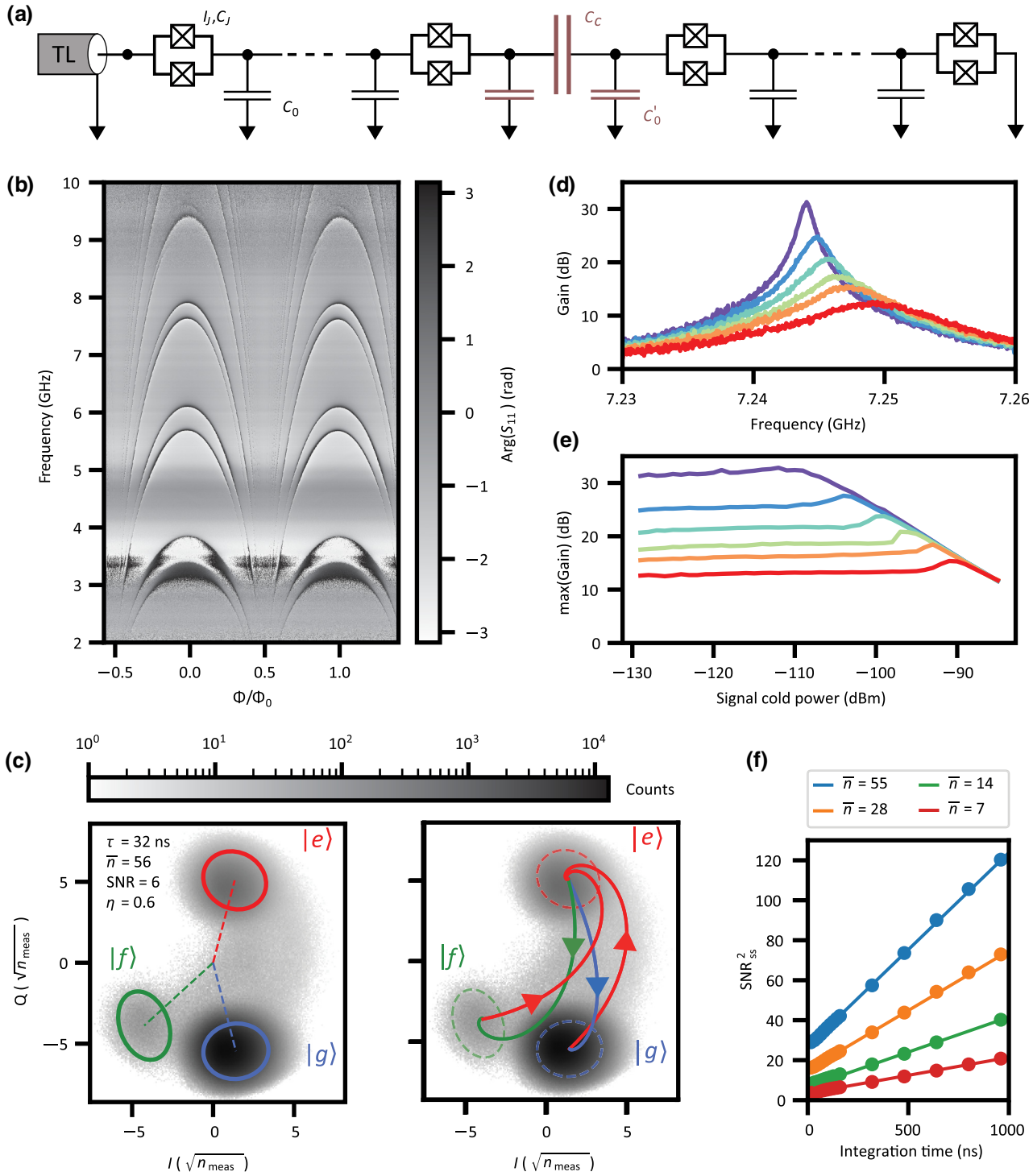

FIG. 4. (a) The circuit diagram of the DJJAA. It consists of an array of identical SQUIDs interrupted in the middle with a series capacitor. The array is galvanically connected to a transmission line (TL). (b) The argument of the reflection coefficient of the weak probe signal versus the external magnetic flux and frequency. (c) 2D histograms of measured I and Q quadratures using the same data as in Fig. 1(c). The ellipses indicate the 2σ areas for the $|g\rangle$, $|e\rangle$, and $|f\rangle$ steady states. The dotted lines in the left-hand panel show the location of the steady-state pointer states α_i, with $i \in \{|g\rangle, |e\rangle, |f\rangle\}$, and the arrowed colored curves in the right-hand figure indicate resonator classical trajectories to a steady state of corresponding color. (d) The power gain versus the signal frequency for different pump powers. (e) The saturation power of the DJJAA operated at different maximum-power-gain values. The gray lines mark readout powers corresponding to $\bar{n} = 56$ (dotted line) and the readout-resonator bifurcation power $\bar{n} = 200$ (straight line). (f) The squared steady-state SNR [Eq. (A1)] as a function of the integration time for different $\bar{n}$. The straight lines are linear fits used to extract a measurement efficiency $\eta = 0.6 \pm 0.1$, with the main source of uncertainty being the photon number calibration.

APPENDIX B: READOUT-RESONATOR NONLINEARITY

The steady states are visibly squeezed because the readout signal effectively acts as a pump to the nonlinear readout resonator, squeezing the vacuum noise, similar to a parametric amplifier. This happens due to the intrinsic nonlinearity [50] $K^{\mathrm{grAl}}/2\pi = -2.4$ kHz of the grAl readout resonator and the inherited state-dependent nonlinearities [56] $K^{|g\rangle}/2\pi = -2.6$ Hz, $K^{|e\rangle}/2\pi = 2$ kHz and $K^{|f\rangle}/2\pi = -2$ kHz at $\bar{n} = 50$ (see Ref. [38]). Note that for the $|e\rangle$ state, the Kerr coefficients almost cancel out, as evidenced by the reduced squeezing of the $|e\rangle$ pointer state in Fig. 4(c).

Due to squeezing, the effective readout SNR can, generally speaking, either increase or decrease. For the situation shown in Fig. 5(a), when the $|g\rangle \rightarrow |e\rangle$ trajectory is mostly visible in the phase response, state separation can be enhanced if the steady states are squeezed along the imaginary axis [Fig. 5(b)]. On the other hand, squeezing along the real axis decreases the effective SNR [Fig. 5(c)].

Since the squeezing axis depends on the readout frequency and readout power, the situation illustrated in Fig. 5(c) can be improved by changing the readout-signal frequency. This improvement, however, is only possible when one is interested in the discrimination of two states. If there are three or more states in the IQ plane, it is difficult, if not impossible, to optimize the squeezing axis for all trajectories.

APPENDIX C: LATCHING AND BAYESIAN FILTERING

The latching filter is designed to declare a jump when a pointer state enters the 2σ area [Fig. 4(c)] of a respective steady state. The detection time (for both latching and Bayesian filtering) is defined as time between leaving the 2σ area of the previous coherent state and jump detection.

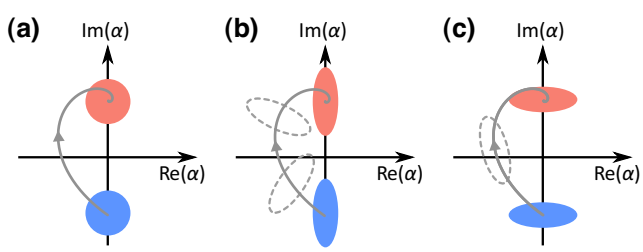

FIG. 5. Sketches of the pointer states of a readout resonator coupled to a two-level system. The red-color pointer states correspond to the excited state and the blue to the ground. The gray arrowed line depicts a classical trajectory from the ground to the excited state. The pointer state is either coherent (a) or squeezed (b),(c), where the squeezing axis is aligned with the imaginary and the real axis, respectively, depending on the readout frequency and readout power. The gray dashed ellipses in (b) and (c) illustrate rotation of the squeezing axis of the pointer state during its evolution along the readout-resonator classical trajectory.

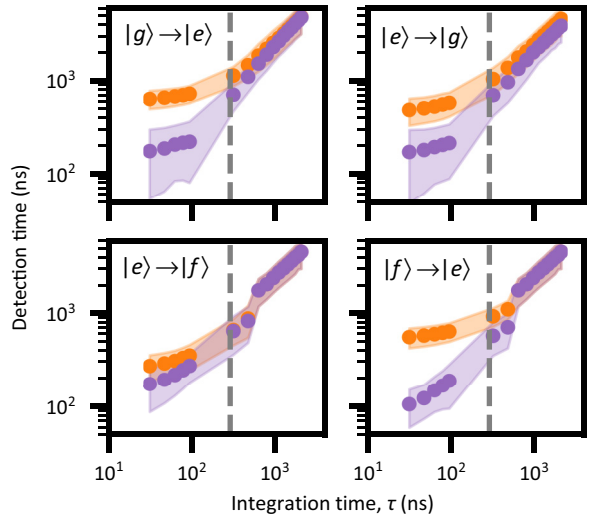

FIG. 6. The average detection time for $|g\rangle \rightarrow |e\rangle$, $|e\rangle \rightarrow |g\rangle$, $|e\rangle \rightarrow |f\rangle$, and $|f\rangle \rightarrow |e\rangle$ jumps as a function of the integration time, obtained using the three-point latching (in orange) or the recursive Bayesian filter (in purple). The transparent areas represent the standard deviation of the jump-detection-time distribution. The gray dashed line corresponds to τ_B.

The Bayesian filtering utilizes the fact that the state of the quantum system is encoded in the instantaneous evolution of the pointer state. The pointer state follows classical trajectories and the expected position of the pointer state $\alpha^{\mathrm{calc}}_{t+\tau}(\alpha_t, H)$ can be calculated for each fluxonium state hypothesis H:

$$\alpha^{\mathrm{calc}}_{t+\tau}(\alpha_t, H) = (\alpha_t - A_H)e^{-\kappa\tau/2+i(\omega_{\mathrm{drive}}-\omega_H)\tau} + A_H. \quad \text{(C1)}$$

Here, α_t is the measured pointer state at time t, A_H is the steady state of the system, ω_{drive} is the readout drive frequency, and ω_H is the state-dependent readout-resonator

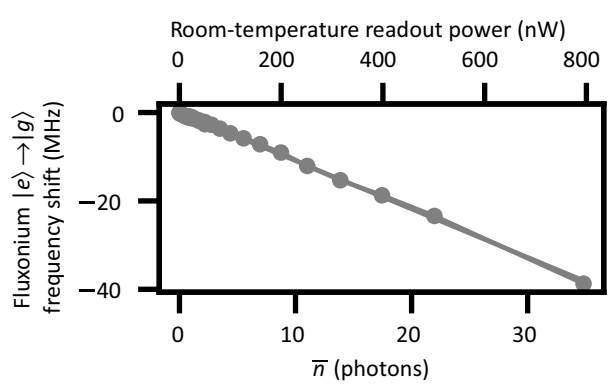

FIG. 7. The measured ac Stark shift plotted versus the room-temperature readout power (top axis) and the corresponding calibrated photon number (bottom axis).

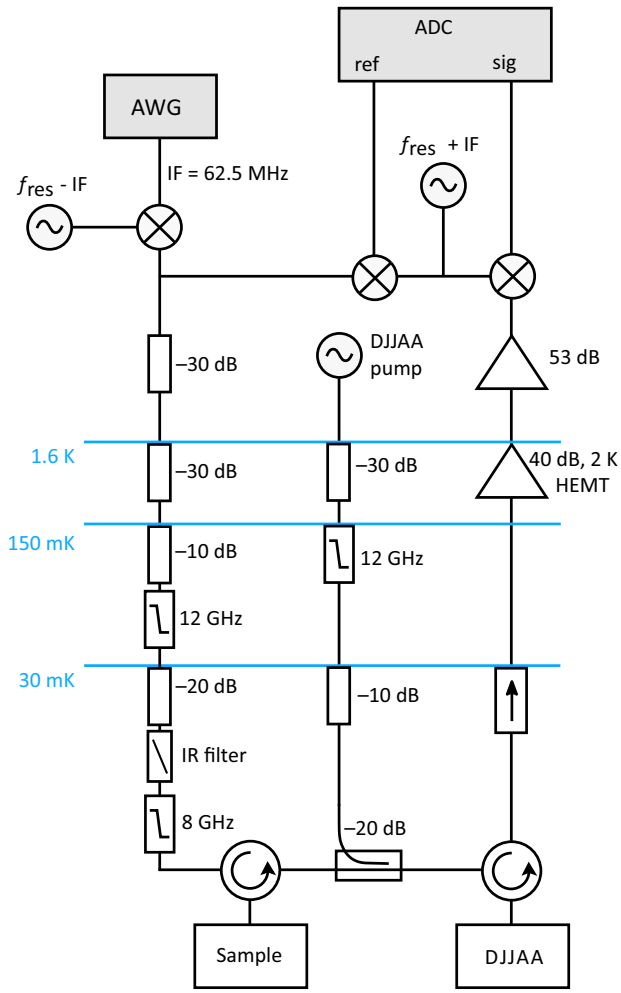

FIG. 8. The schematics of the measurement setup. The displayed microwave components are thermalized to the nearest temperature stage indicated above them. The readout chain uses a commercial two-channel microwave generator operated in continuous wave mode in addition to a channel of a commercial arbitrary waveform generator (AWG) in an interferometric configuration. First, the readout pulse at an intermediate frequency (IF) = 62.5 MHz is upconverted to the readout frequency and split into two signals. One signal is directly measured with the analog digital converter (ADC), whereas the other signal first passes through the cryostat.

frequency. This expression can be used for the calculation of the pointer-state evolution for the Bayesian inference [Eq. (3)] and gives a time scale for the time evolution of the discrimination between quantum states. However, one should keep in mind that each trajectory in the *I*-*Q* space is different, depending on the readout frequency and power, and some of them might even intersect.

If the angle between pointer states is big enough, it is also possible to make a more robust approximation and only track the phase (or a quadrature), assuming that it evolves as

$$\varphi_{t+\tau}^{\mathrm{calc}}(\varphi_t, H) \approx (\varphi_t - \phi_H)e^{-C_H\kappa\tau/2} + \phi_H. \tag{C2}$$

Here, φ_t is the measured phase at time t, ϕ_H is the phase of the respective steady state, and $C_H = 1 \pm 0.2$ an empirical coefficient accounting for the resonator nonlinearity and for the term $e^{i(\omega_{\mathrm{drive}}-\omega_H)\tau}$ in Eq. (C1). Both the pointer-state evolution [Eq. (C1)] and the exponential-phase evolution [Eq. (C2)] show similar results when used for the Bayesian filtering and in this work we utilize the simpler Eq. (C2) to calculate the expected phase $\varphi_{t+\tau}^{\mathrm{calc}}$ for Eq. (3).

APPENDIX D: PHOTON-NUMBER CALIBRATION

The photon-number calibration for the readout is performed using the measured ac Stark shift [57] (see Fig. 7). For each room-temperature continuous-wave resonator drive power P_{RO}, the qubit frequency shift $\Delta f_{\mathrm{ge}}(P_{\mathrm{RO}}) = \chi_{\mathrm{ge}}\bar{n}/2\pi$ is measured. Thus it is possible to link the room-temperature drive power and the circulating photon number $\bar{n}$.

APPENDIX E: MEASUREMENT SETUP

The measurement setup is shown in Fig. 8. In front of the analog-to-digital converter, we use band-pass filters with a bandwidth of 10 MHz. An additional postprocessing filtering with a bandwidth of 4 MHz is applied to the signal trace.

[1] W. Nagourney, J. Sandberg, and H. Dehmelt, Shelved Optical Electron Amplifier: Observation of Quantum Jumps, Phys. Rev. Lett. **56**, 2797 (1986).
[2] P. Neumann, J. Beck, M. Steiner, F. Rempp, H. Fedder, P. R. Hemmer, J. Wrachtrup, and F. Jelezko, Single-shot readout of a single nuclear spin, Science **329**, 542 (2010).
[3] L. Robledo, L. Childress, H. Bernien, B. Hensen, P. F. A. Alkemade, and R. Hanson, High-fidelity projective readout of a solid-state spin quantum register, Nature **477**, 574 (2011).
[4] S. Gleyzes, S. Kuhr, C. Guerlin, J. Bernu, S. Deléglise, U. B. Hoff, M. Brune, J.-M. Raimond, and S. Haroche, Quantum jumps of light recording the birth and death of a photon in a cavity, Nature **446**, 297 (2007).
[5] F. Jelezko, I. Popa, A. Gruber, C. Tietz, J. Wrachtrup, A. Nizovtsev, and S. Kilin, Single spin states in a defect center resolved by optical spectroscopy, Appl. Phys. Lett. **81**, 2160 (2002).
[6] R. Vijay, D. H. Slichter, and I. Siddiqi, Observation of Quantum Jumps in a Superconducting Artificial Atom, Phys. Rev. Lett. **106**, 110502 (2011).
[7] M. D. Reed, L. DiCarlo, S. E. Nigg, L. Sun, L. Frunzio, S. M. Girvin, and R. J. Schoelkopf, Realization of three-qubit quantum error correction with superconducting circuits, Nature **482**, 382 (2012).

[8] D. Ristè, M. Dukalski, C. A. Watson, G. de Lange, M. J. Tiggelman, Y. M. Blanter, K. W. Lehnert, R. N. Schouten, and L. DiCarlo, Deterministic entanglement of superconducting qubits by parity measurement and feedback, Nature **502**, 350 (2012).

[9] L. Sun, A. Petrenko, Z. Leghtas, B. Vlastakis, G. Kirchmair, K. M. Sliwa, A. Narla, M. Hatridge, S. Shankar, J. Blumoff, L. Frunzio, M. Mirrahimi, M. H. Devoret, and R. J. Schoelkopf, Tracking photon jumps with repeated quantum non-demolition parity measurements, Nature **511**, 444 (2014).

[10] J. Kelly *et al.*, State preservation by repetitive error detection in a superconducting quantum circuit, Nature **519**, 66 (2015).

[11] N. Ofek, A. Petrenko, R. Heeres, P. Reinhold, Z. Leghtas, B. Vlastakis, Y. Liu, L. Frunzio, S. Girvin, L. Jiang, M. Mirrahimi, M. Devoret, and R. Schoelkopf, Extending the lifetime of a quantum bit with error correction in superconducting circuits, Nature **536**, 441 (2016).

[12] D. Riste, C. C. Bultink, M. J. Tiggelman, R. N. Schouten, K. W. Lehnert, and L. DiCarlo, Millisecond charge-parity fluctuations and induced decoherence in a superconducting transmon qubit, Nat. Commun. **4**, 1913 (2013).

[13] U. Vool, I. M. Pop, K. Sliwa, B. Abdo, C. Wang, T. Brecht, Y. Y. Gao, S. Shankar, M. Hatridge, G. Catelani, M. Mirrahimi, L. Frunzio, R. J. Schoelkopf, L. I. Glazman, and M. H. Devoret, Non-Poissonian Quantum Jumps of a Fluxonium Qubit due to Quasiparticle Excitations, Phys. Rev. Lett. **113**, 247001 (2014).

[14] K. Serniak, S. Diamond, M. Hays, V. Fatemi, S. Shankar, L. Frunzio, R. Schoelkopf, and M. Devoret, Direct Dispersive Monitoring of Charge Parity in Offset-Charge-Sensitive Transmons, Phys. Rev. Appl. **12**, 014052 (2019).

[15] A. Wallraff, D. I. Schuster, A. Blais, L. Frunzio, R. S. Huang, J. Majer, S. Kumar, S. M. Girvin, and R. J. Schoelkopf, Strong coupling of a single photon to a superconducting qubit using circuit quantum electrodynamics, Nature **431**, 162 (2004).

[16] P. Krantz, M. Kjaergaard, F. Yan, T. P. Orlando, S. Gustavsson, and W. D. Oliver, A quantum engineer's guide to superconducting qubits, Appl. Phys. Rev. **6**, 021318 (2019).

[17] A. Blais, S. M. Girvin, and W. D. Oliver, Quantum information processing and quantum optics with circuit quantum electrodynamics, Nat. Phys. **16**, 247 (2020).

[18] M. Kjaergaard, M. E. Schwartz, J. Braumüller, P. Krantz, J. I. Wang, S. Gustavsson, and W. D. Oliver, Superconducting qubits: Current state of play, Annu. Rev. Condens. Matter Phys. **11**, 369 (2020).

[19] E. Jeffrey, D. Sank, J. Y. Mutus, T. C. White, J. Kelly, R. Barends, Y. Chen, Z. Chen, B. Chiaro, A. Dunsworth, A. Megrant, P. J. J. O'Malley, C. Neill, P. Roushan, A. Vainsencher, J. Wenner, A. N. Cleland, and J. M. Martinis, Fast Accurate State Measurement with Superconducting Qubits, Phys. Rev. Lett. **112**, 190504 (2014).

[20] C. C. Bultink, M. A. Rol, T. E. O'Brien, X. Fu, B. C. S. Dikken, C. Dickel, R. F. L. Vermeulen, J. C. de Sterke, A. Bruno, R. N. Schouten, and L. DiCarlo, Active Resonator Reset in the Nonlinear Dispersive Regime of Circuit QED, Phys. Rev. Appl. **6**, 034008 (2016).

[21] T. Walter, P. Kurpiers, S. Gasparinetti, P. Magnard, A. Potočnik, Y. Salathé, M. Pechal, M. Mondal, M. Oppliger, C. Eichler, and A. Wallraff, Rapid High-Fidelity Single-Shot Dispersive Readout of Superconducting Qubits, Phys. Rev. Appl. **7**, 054020 (2017).

[22] R. Dassonneville, T. Ramos, V. Milchakov, L. Planat, E. Dumur, F. Foroughi, J. Puertas, S. Leger, K. Bharadwaj, J. Delaforce, C. Naud, W. Hasch-Guichard, J. J. García-Ripoll, N. Roch, and O. Buisson, Fast High-Fidelity Quantum Nondemolition Qubit Readout via a Nonperturbative Cross-Kerr Coupling, Phys. Rev. X **10**, 011045 (2020).

[23] M. A. Castellanos-Beltran and K. W. Lehnert, Widely tunable parametric amplifier based on a superconducting quantum interference device array resonator, Appl. Phys. Lett. **91**, 083509 (2007).

[24] T. Yamamoto, K. Inomata, M. Watanabe, K. Matsuba, T. Miyazaki, W. D. Oliver, Y. Nakamura, and J. S. Tsai, Flux-driven Josephson parametric amplifier, Appl. Phys. Lett. **93**, 042510 (2008).

[25] J. Mutus, T. White, R. Barends, Y. Chen, Z. Chen, B. Chiaro, A. Dunsworth, E. Jeffrey, J. Kelly, A. Megrant, C. Neill, P. O'Malley, P. Roushan, D. Sank, A. Vainsencher, J. Wenner, K. Sundqvist, A. Cleland, and J. Martinis, Strong environmental coupling in a Josephson parametric amplifier, Appl. Phys. Lett. **104**, 263513 (2014).

[26] N. Roch, E. Flurin, F. Nguyen, P. Morfin, P. Campagne-Ibarcq, M. H. Devoret, and B. Huard, Widely Tunable, Nondegenerate Three-Wave Mixing Microwave Device Operating near the Quantum Limit, Phys. Rev. Lett. **108** (2012).

[27] C. Eichler and A. Wallraff, Controlling the dynamic range of a Josephson parametric amplifier, EPJ Quantum Technol. **1**, 2 (2014).

[28] C. Macklin, K. O'Brien, D. Hover, M. Schwartz, V. Bolkhovsky, X. Zhang, W. Oliver, and I. Siddiqi, A near-quantum-limited Josephson traveling-wave parametric amplifier, Science (New York, N.Y.) **350**, 307 (2015).

[29] A. Roy and M. Devoret, Introduction to parametric amplification of quantum signals with Josephson circuits, C. R. Phys. **17**, 740 (2016).

[30] C. M. Caves, Quantum limits on noise in linear amplifiers, Phys. Rev. D **26**, 1817 (1982).

[31] J. E. Johnson, C. Macklin, D. H. Slichter, R. Vijay, E. B. Weingarten, J. Clarke, and I. Siddiqi, Heralded State Preparation in a Superconducting Qubit, Phys. Rev. Lett. **109**, 050506 (2012).

[32] D. Sank *et al.*, Measurement-Induced State Transitions in a Superconducting Qubit: Beyond the Rotating Wave Approximation, Phys. Rev. Lett. **117**, 190503 (2016).

[33] Z. K. Minev, S. O. Mundhada, S. Shankar, P. Reinhold, R. Gutiérrez-Jáuregui, R. J. Schoelkopf, M. Mirrahimi, H. J. Carmichael, and M. H. Devoret, To catch and reverse a quantum jump mid-flight, Nature **570**, 200 (2019).

[34] M. Boissonneault, J. M. Gambetta, and A. Blais, Dispersive regime of circuit QED: Photon-dependent qubit dephasing and relaxation rates, Phys. Rev. A **79**, 013819 (2009).

[35] M. Malekakhlagh, A. Petrescu, and H. E. Türeci, Lifetime renormalization of weakly anharmonic superconducting qubits. I. Role of number nonconserving terms, Phys. Rev. B **101**, 134510 (2020).

[36] A. Petrescu, M. Malekakhlagh, and H. E. Türeci, Lifetime renormalization of driven weakly anharmonic superconducting qubits. II. The readout problem, Phys. Rev. B **101**, 134510 (2020).

[37] L. Grünhaupt, M. Spiecker, D. Gusenkova, N. Maleeva, S. T. Skacel, I. Takmakov, F. Valenti, P. Winkel, H. Rotzinger, A. V. Ustinov, and I. M. Pop, Granular aluminium as a superconducting material for high-impedance quantum circuits, Nat. Mater. **18**, 816 (2019).

[38] D. Gusenkova, M. Spiecker, R. Gebauer, M. Willsch, D. Willsch, F. Valenti, N. Karcher, L. Grünhaupt, I. Takmakov, P. Winkel, D. Rieger, A. V. Ustinov, N. Roch, W. Wernsdorfer, K. Michielsen, O. Sander, and I. M. Pop, Quantum Nondemolition Dispersive Readout of a Superconducting Artificial Atom Using Large Photon Numbers, Phys. Rev. Appl. **15**, 064030 (2021).

[39] P. Winkel, I. Takmakov, D. Rieger, L. Planat, W. Hasch-Guichard, L. Grünhaupt, N. Maleeva, F. Foroughi, F. Henriques, K. Borisov, J. Ferrero, A. V. Ustinov, W. Wernsdorfer, N. Roch, and I. M. Pop, Nondegenerate Parametric Amplifiers Based on Dispersion-Engineered Josephson-Junction Arrays, Phys. Rev. Appl. **13**, 024015 (2020).

[40] A. N. Korotkov, Quantum Bayesian approach to circuit QED measurement with moderate bandwidth, Phys. Rev. A **94**, 042326 (2016).

[41] P. Wang, L. Qin, and X.-Q. Li, Quantum Bayesian rule for weak measurements of qubits in superconducting circuit QED, New J. Phys. **16**, 123047 (2014).

[42] S. J. Weber, K. W. Murch, M. E. Kimchi-Schwartz, N. Roch, and I. Siddiqi, Quantum trajectories of superconducting qubits, C. R. Phys. **17**, 766 (2016).

[43] W. Feng, P. Liang, L. Qin, and X.-Q. Li, Exact quantum Bayesian rule for qubit measurements in circuit QED, Sci. Rep. **6**, 20492 (2016).

[44] S. Reick, K. Mølmer, W. Alt, M. Eckstein, T. Kampschulte, L. Kong, R. Reimann, A. Thobe, A. Widera, and D. Meschede, Analyzing quantum jumps of one and two atoms strongly coupled to an optical cavity, J. Opt. Soc. Am. B **27**, A152 (2010).

[45] P. Six, P. Campagne-Ibarcq, I. Dotsenko, A. Sarlette, B. Huard, and P. Rouchon, Quantum state tomography with noninstantaneous measurements, imperfections, and decoherence, Phys. Rev. A **93**, 012109 (2016).

[46] V. E. Manucharyan, J. Koch, L. I. Glazman, and M. H. Devoret, Fluxonium: Single Cooper-pair circuit free of charge offsets, Science **326**, 113 (2009).

[47] Y.-H. Lin, L. B. Nguyen, N. Grabon, J. San Miguel, N. Pankratova, and V. E. Manucharyan, Demonstration of Protection of a Superconducting Qubit from Energy Decay, Phys. Rev. Lett. **120**, 150503 (2018).

[48] A. Kou, W. Smith, U. Vool, I. Pop, K. Sliwa, M. Hatridge, L. Frunzio, and M. Devoret, Simultaneous Monitoring of Fluxonium Qubits in a Waveguide, Phys. Rev. Appl. **9**, 064022 (2018).

[49] C. Eichler, Y. Salathe, J. Mlynek, S. Schmidt, and A. Wallraff, Quantum-Limited Amplification and Entanglement in Coupled Nonlinear Resonators, Phys. Rev. Lett. **113**, 110502 (2014).

[50] N. Maleeva, L. Grünhaupt, T. Klein, F. Levy-Bertrand, O. Dupré, M. Calvo, F. Valenti, P. Winkel, F. Friedrich, W. Wernsdorfer, A. V. Ustinov, H. Rotzinger, A. Monfardini, M. V. Fistul, and I. M. Pop, Circuit quantum electrodynamics of granular aluminum resonators, Nat. Commun. **9**, 3889 (2018).

[51] D. H. Slichter, Ph.D. thesis, University of California, Berkeley, 2011, https://digitalassets.lib.berkeley.edu/etd/ucb/text/Slichter_berkeley_0028E_11889.pdf.

[52] S. Touzard, A. Kou, N. Frattini, V. Sivak, S. Puri, A. Grimm, L. Frunzio, S. Shankar, and M. Devoret, Gated Conditional Displacement Readout of Superconducting Qubits, Phys. Rev. Lett. **122**, 080502 (2019).

[53] P. Krantz, A. Bengtsson, M. Simoen, S. Gustavsson, V. Shumeiko, W. D. Oliver, C. M. Wilson, P. Delsing, and J. Bylander, Single-shot read-out of a superconducting qubit using a Josephson parametric oscillator, Nat. Commun. **7**, 11417 (2016).

[54] R. Gebauer, N. Karcher, D. Gusenkova, M. Spiecker, L. Grünhaupt, I. Takmakov, P. Winkel, L. Planat, N. Roch, W. Wernsdorfer, A. V. Ustinov, M. Weber, M. Weides, I. M. Pop, and O. Sander, State preparation of a fluxonium qubit with feedback from a custom FPGA-based platform, AIP Conference Proc. **2241**, 020015 (2020).

[55] https://www.quantum-machines.com.

[56] W. C. Smith, A. Kou, U. Vool, I. M. Pop, L. Frunzio, R. J. Schoelkopf, and M. H. Devoret, Quantization of inductively shunted superconducting circuits, Phys. Rev. B **94**, 144507 (2016).

[57] D. I. Schuster, A. Wallraff, A. Blais, L. Frunzio, R.-S. Huang, J. Majer, S. M. Girvin, and R. J. Schoelkopf, AC Stark Shift and Dephasing of a Superconducting Qubit Strongly Coupled to a Cavity Field, Phys. Rev. Lett. **94**, 123602 (2005).